Supplemental Material:

**Excitation Dependent Fano-like Interference Effects in Plasmonic Silver Nanorods**

S. M. Collins, O. Nicoletti, D. Rossouw, T. Ostasevicius, P. A. Midgley

This supplemental material contains additional figures and text related to processing of experimental data and interpretation of simulated data and model fitting presented in the main text. The supplemental material is organized in the following sections:

1. NMF Processing

Figure S1 presents unprocessed NMF results as spectral factors and the corresponding spatial distribution maps. The order of the components indicates the significance relative to the noise level (Factor 8 of Rod A is a noise component, retained to also include Factor 9 which corresponds to the $m = 6$ resonance). The retention of this component gives rise to a minor inflection of Factor 1 near 1.0 eV in the spectra (Fig. S1(a)). The sum of Factors 1 and 8 reproduces the zero loss peak (ZLP) as depicted in Fig. 2 (main text).
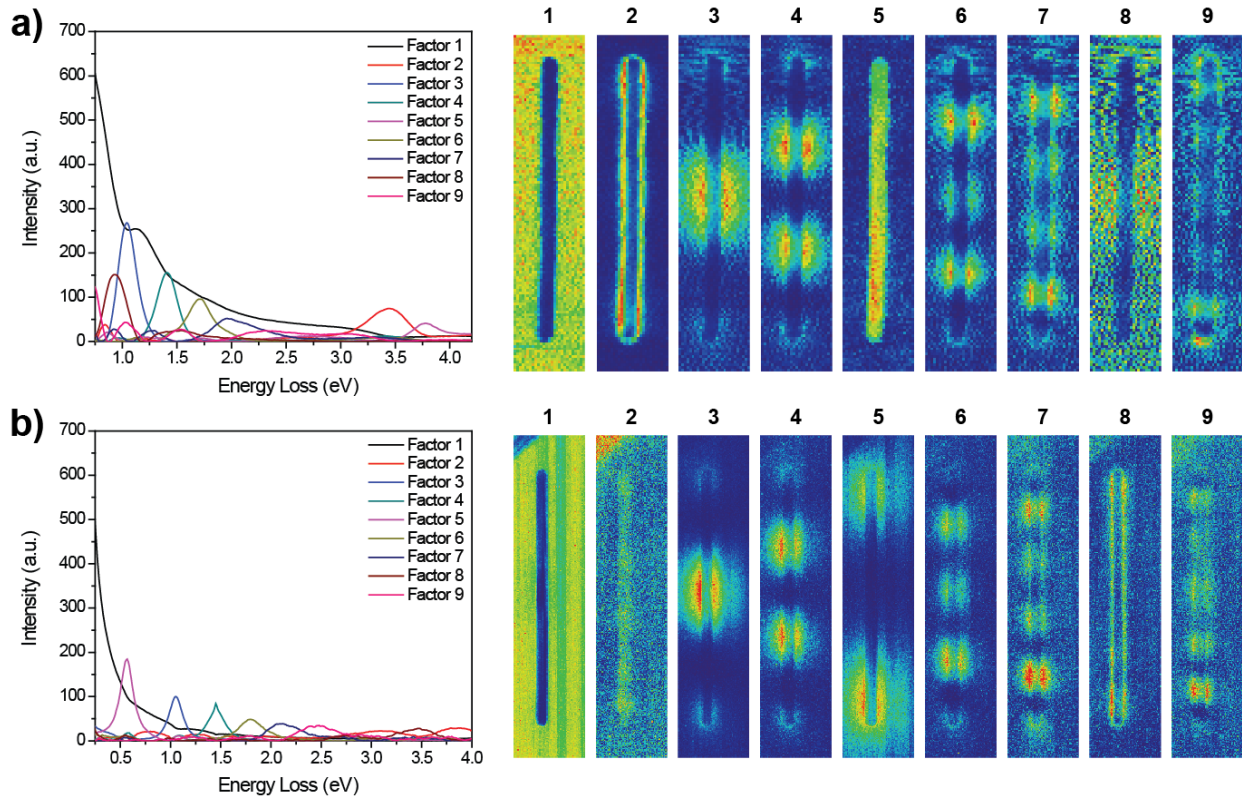
Figure S1. Unprocessed NMF components for (a) Rod A and (b) Rod B represented in spectral and map form.

In Fig. S1(b), Factor 2 describes the bulk plasmon at approximately 3.8 eV. The factor also includes some spectral signal at 3 eV, likely partial signal from higher order modes beyond $m = 6$ giving rise to slightly enhanced intensity in the bulk plasmon map near the rod tips.

To account for varying intensity of the zero loss peak (ZLP) in order to compare with simulated energy loss probabilities, raw component maps were subsequently divided pixel by pixel by the component map for Factor 1, the component corresponding to the ZLP. As an alternative, component maps could be divided by the ZLP intensity in the original spectrum image. Figure S2 presents such maps for modes $m = 4$ and $m = 5$ for Rod A and Rod B and a comparison of experimental and simulated line profiles. The observed amplitude modulation is reproduced using either processing procedure, and the line profiles likewise match the simulated line profiles as in Fig. 3.
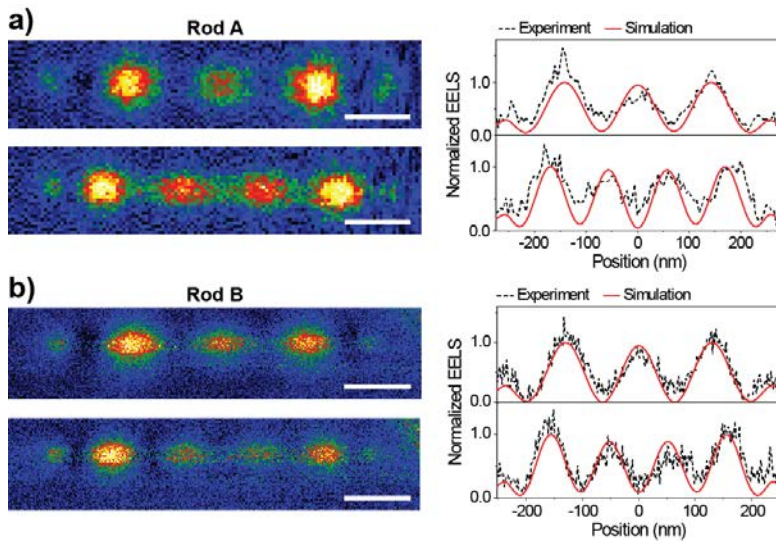
Figure S2. Zero loss peak normalization using the pixel-by-pixel zero loss peak amplitude extracted from the spectrum image as an alternative to the pixel-by-pixel amplitude of the zero loss peak component extracted from NMF (Fig. 3). (a)-(b) STEM-EELS maps and line profiles (4 nm from rod side) of modal components $m = 4$ and 5 for (a) Rod A and (b) Rod B. Extracted experimental line profiles are compared with simulated line profiles calculated by DDA methods.

Figure S3 presents spectra at three key points along Rod A at the $m = 5$ resonance (mode maximum at 1.98 eV in these simulations). The peak shape remains unchanged for these points along the rod, corresponding to the observed similar amplitude modulation across the resonance in Fig. 6.
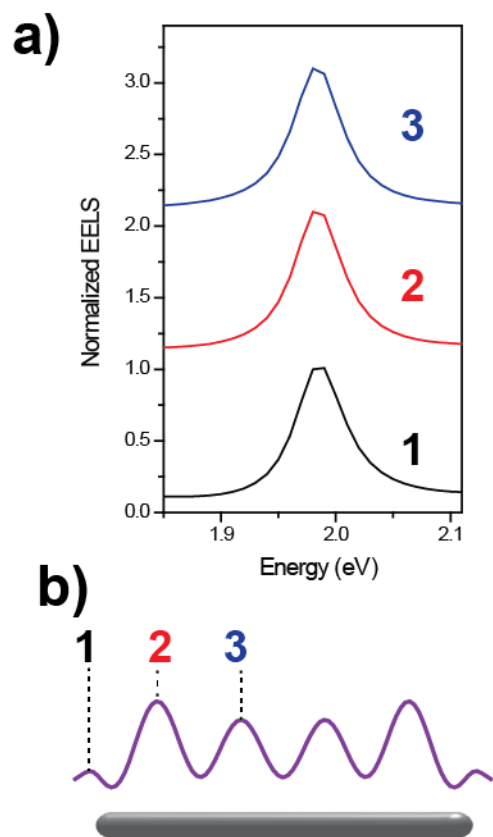
Figure S3. (a) EELS spectra simulated using DDA at the $m = 5$ mode for key trajectories along Rod A indicated in (b).

2. Substrate and Instrument Effects

To further explore the role of the substrate and instrument effects, additional simulations on Rod A are presented in Fig. S6. Fig. S6(a)-(b) presents line profiles with and without a substrate (30 nm silicon nitride membrane). In each case, integrated peak areas determined from peak fitting were compared as in Fig. 3. For simulations without a substrate, a constant effective refractive index of the medium was used to reproduce the red-shifting of modes due to the substrate and to match the resonances to the same energy range of the Ag dielectric function. Instrumental broadening effects were also taken into consideration, modeled as a convolution of finely stepped simulations (0.01 eV step) with a Gaussian function. In EELS, electrons are emitted with a finite energy spread, observed in the width of the EELS signature of electrons passing through the sample with little or no energy loss: the zero loss peak (ZLP).[1] This intrinsic width of the ZLP gives rise to an experimental broadening of the energy loss spectrum.[1] Though the experimental ZLP is not truly Gaussian, the ZLP is often described in terms of its full width at half maximum (FWHM)[2,3] and a Gaussian function can adequately model the major contributions to ZLP broadening. STEM-EELS of Rod A was acquired with a ZLP of approximately 180 meV FWHM whereas for Rod B, STEM-EELS was acquired with a ZLP of approximately 90 meV FWHM. For pure simulation data, Lorentzian functions were fitted to the peaks as plasmon resonances are, to a good approximation, Lorentzian.[4,5] For broadened simulations, Voigt functions were fitted to the peaks, as a convolution of Lorentzian and Gaussian functions. This processing method using related functional forms illustrates the extent to which the underlying signal is recoverable by peak decomposition approaches in EELS.

In the event of significant intrinsic or instrumental broadening, incoherent summation effects between adjacent modes may alter the observed amplitudes in line profiles. Peak fitting

procedures can remove these effects completely if conducted appropriately. In Fig. S6(a)-(b), the Lorentzian and Voigt function fits for peaks corresponding to modes $m = 4$ and $m = 5$ show good correspondence between pure and broadened simulated line profiles. For each pair of simulations with and without a substrate, the pure and broadened line profiles are nearly superimposed. Small differences likely arise from incomplete modeling of the peaks using numerical fitting procedures with simple Lorentzian and Gaussian functions. Simulation noise (arising from the use of a numerical iterative solver) and minor artifacts in the simulated energy loss spectra (see also Fig. S7 and associated discussion) may give rise to these slight differences in integrated areas determined by numerical fitting when comparing pure and broadened spectra.

The simulations with a substrate exhibit lower relative intensity at the central antinodes than simulations without a substrate. However, the amplitude modulation present in the simulations without a substrate demonstrates that amplitude modulation is not a substrate-induced effect. The effect of the substrate in the induced near field is depicted in Fig. S6(c)-(d). The modulus of the induced electric field $|\vec{E}^{ind}|$ is plotted in cross-section at a plane 2 nm from the rod. The electron trajectory is illustrated as the dashed red arrow for reference. The induced near field intensity in the case of the rod on a substrate is shifted toward the substrate as expected.[6,7] The intensity as a function of distance from the electron trajectory also falls off more rapidly, consistent with enhanced damping induced by the substrate. The role of intensity damping is key in the case of the observed EELS response and the amplitude modulation (see also Fig. S12-S13 and discussion). These effects have been reported previously for nanorods.[6,7] Figure S6(e) presents the ratio of EELS intensity at the central antinodes and the maximum EELS intensity for mode $m = 5$ as a function of impact parameter (distance between the electron trajectory and the rod side) for simulations with and without a substrate. The observed ratio of

antinode intensity changes as a function of impact parameter. Effectively, the central antinode intensity decays more rapidly than the maximal signal. This trend is consistent with weaker fields and correspondingly less charge on the surface at the central antinodes. While the ratio is lower with a substrate, the rate of change is equal for both cases. The substrate gives rise to a weaker surface plasmon response overall, resulting in a lower ratio of intensity at the central and outer antinodes. This consistency further reinforces the independence of amplitude modulation and substrate effects. The substrate predominantly serves to dampen the fields and consequently weaken the EELS signal.

Notably, STEM-EELS studies of nanorods at lower accelerating voltage have exhibited limited amplitude modulation.[8] These reports examined significantly longer wires with modes red-shifted to lower energies.[8] Interference effects are expected to be more pronounced for more closely spaced modes at higher energy. The inelastic cross-section for lower energy electrons is also much higher,[1] and so, as in the discussion of damping and trajectory effects (Fig. S6, S12, S13), the modulated contribution to the signal will be reduced and consequently less observable amplitude modulation is expected. Additionally, lower energy electrons interact more locally with plasmonic nanoparticles,[9] and the interference phenomena described here are long-range effects.

Some authors have suggested that symmetry breaking by a substrate might allow for interaction of "bright" and "dark" modes.[10] The simulations and experiments presented here indicate no such substrate-induced effect. The addition of a substrate does not alter the critical mirror plane symmetry element in the nanorod. Symmetry-breaking, as with reported STEM-EELS on "nanocarrot" geometries, may alter the necessary symmetry elements.[11]
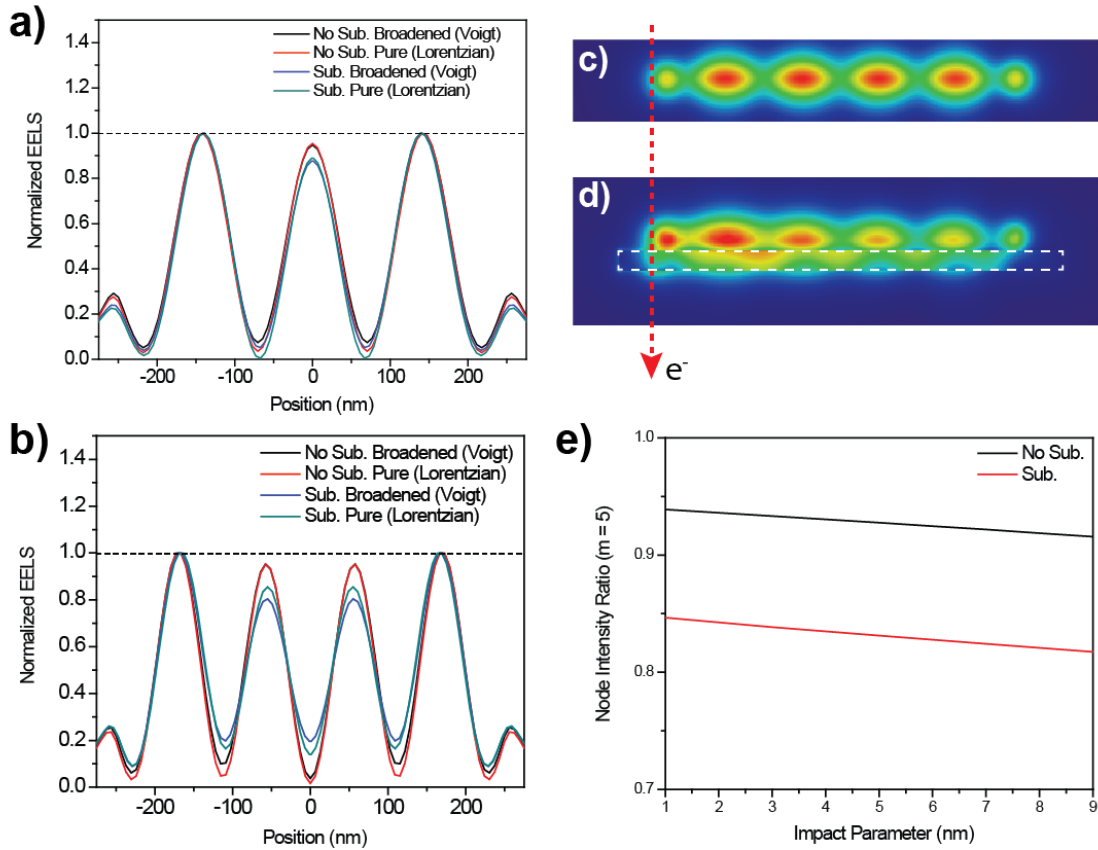
Figure S4. Comparison of simulations of Rod A with and without a 30 nm thick silicon nitride substrate considering ZLP broadening effects. Line profiles for (a) mode $m = 4$ and (b) mode $m = 5$ are shown using peak fitting for Lorentzian peaks (pure simulation) and Voigt peaks (simulation convolved with a Gaussian of equivalent width to the experimental ZLP) for simulations with and without a substrate. The near field $|\vec{E}^{ind}|$ (c) without a substrate and (d) with the 30 nm thick silicon nitride substrate is plotted in cross-section at a plane 2 nm from the rod edge for an electron trajectory at the rod end (dashed red arrow). (e) The ratio of central antinode intensity to maximum antinode intensity for $m = 5$ simulations with and without a substrate.

3. DDA Discretization

In order for computationally feasible DDA simulations of line profiles, in particular for line profile modeling with peak fitting requiring very fine energy steps over a broad energy range, DDA simulations for Fig. 3-4 were performed with 2 nm dipole spacing (see also Sec. II). Calculations for Fig. 7 and Fig. 9 were manageable with 1 nm dipole spacing and provide simulated spectra more suitable for detailed analysis of phase and line shape. Fig. S5 and Fig. S6 present duplicates of Fig. 7 and Fig. 9 calculated with 2 nm dipole spacing.
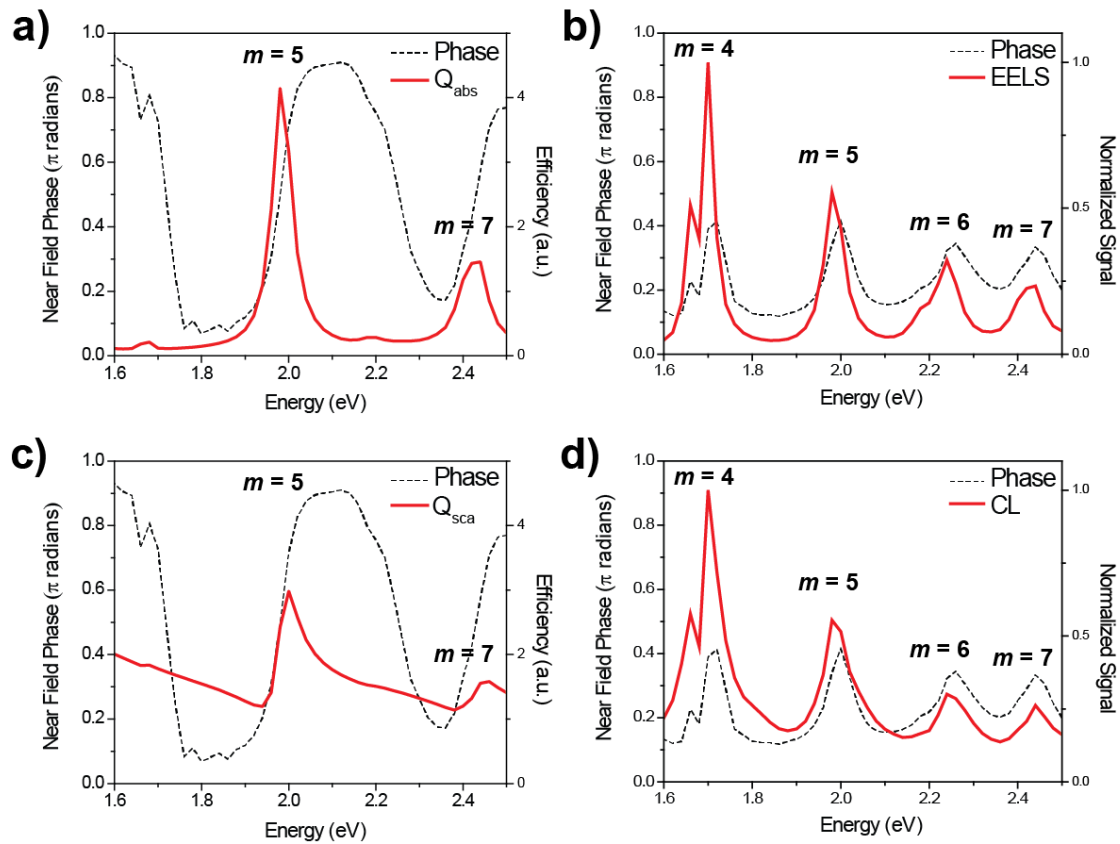
Figure S5. Spectra and phase relationships for (a),(c) plane wave light and (b),(d) electron beam excitation for Rod A (no substrate) simulated by DDA using 2 nm dipole spacing. (a) The light absorption (Q_{abs}) and (c) scattering (Q_{sca}) efficiencies are plotted for plane wave light excitation. (b) The EELS and (d) CL responses are plotted for electron beam excitation. The electron beam was positioned 4 nm from the tip of the rod, and the phase here refers to the phase of the induced field along the axis of the rod (y-axis) at the same offset as the electron trajectory and even with the *xy*-mirror plane (point marked E_y in Fig. 3).

The effects of the coarser 2 nm dipole spacing are generally minor, producing artifacts at particular energies in the spectra (Fig. S5). The artifacts likely arise from faceting of the dipole array. Given ZLP broadening (convolution) and peak fitting procedures for comparison with experiment, these artifacts do not present a significant issue for line profile analysis, nor do they appear to modulate the dipole moment data (Fig. 10-11). Peak positions varied minimally ($<$ 0.02 eV for $m = 5$). Near fields on and near resonance (Fig. S6) show identical observations about amplitude modulation as Fig. 9.
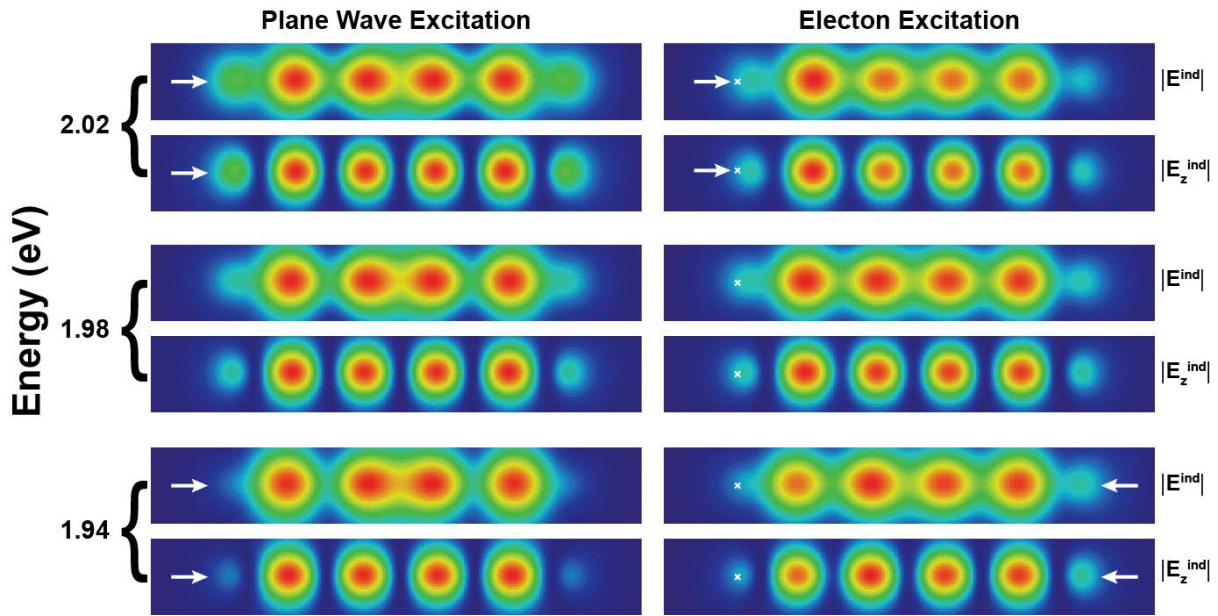
Figure S6. Near field distribution in a plane 40 nm above Rod A (no substrate) simulated by DDA using 2 nm dipole spacing. White crosses mark the electron beam trajectory. Amplitude modulation in the near field along the rod is apparent for both excitations. For plane wave excitation (left), white arrows indicate where the near field intensity changes across the Fano-like resonance from 1.94 to 2.02 eV. For electron excitation (right), white arrows indicate similar near field intensities above and below the resonance energy, but with a shift from one end to the other.

4. Additional Phase Analysis

For trajectories close to the particle (Fig. 7(b),(d)), the negatively charged electron beam strongly polarizes the material closest to the trajectory, and for trajectories close to the rod tip, this partially pins the phase by inducing a local positive charge for all energy losses despite overall phase inversion of the surface plasmon resonance mode. For trajectories further from the rod (Fig. S7), phase inversion from 0 to beyond $-\pi/2$ radians is observed, yet the peaks in EELS remain symmetric. Phase inversion of the plasmon as depicted in Fig. 7(b),(d) and Fig. S7 is insufficient to demonstrate a Fano resonance condition in the energy loss spectra.
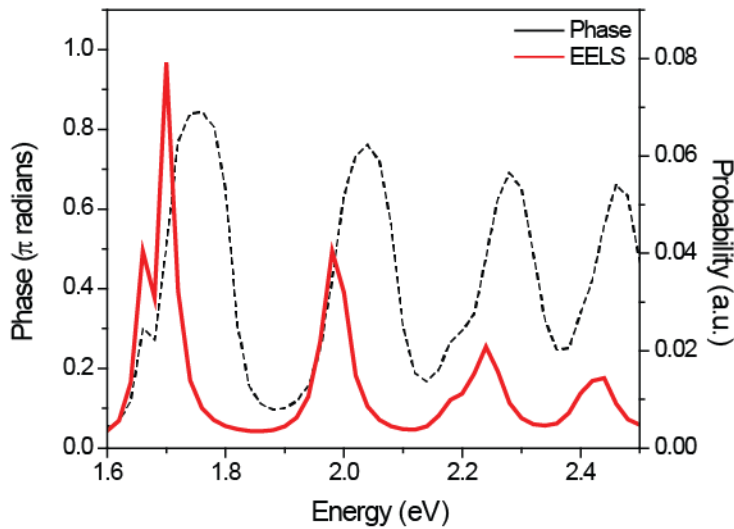
Figure S7. Phase analysis for electron trajectory 22 nm from the tip of Rod A. The corresponding EELS probability is plotted for reference.

5. Damping Effects

Coupling of longitudinal modes in the near field requires modes to be excited with both spatial and spectral overlap.[10] Damping should therefore play a key role in amplitude modulation if amplitude modulation is in fact related to near field coupling and interference. Damping in plasmonic systems is generally considered to consist of linearly additive contributions from radiative and non-radiative processes.[12,13] In DDA simulations, non-radiative damping may be controlled by adjusting the internal damping parameter of a Drude model dielectric function of the form:[14]

$$\varepsilon(\omega) = \varepsilon_\infty - \omega_P^2/(\omega^2 + i\omega\Gamma) \quad \text{(S1)}$$

where ω is the angular frequency, $\varepsilon(\omega)$ is the frequency-dependent dielectric function, ε_∞ incorporates the dielectric response at infinite frequency, ω_P is the plasma frequency, and Γ is the internal damping parameter.

Additional simulations were carried out for a 500 nm long rod with a 10 nm radius and are presented in Fig. S8 (19,955 dipoles, 2 nm dipole spacing). These simulations are qualitatively consistent with the simulations for Rod A. For the $m = 11$ mode for this simulated rod, amplitude modulation decreases with reduced internal damping. The higher mode order provides a good example for reduced radiative damping (weaker dipole moment) and closer mode spacing (stronger coupling). Moreover, the simulation on an additional rod confirms the effect is not unique to a particular set of rod shape parameters. In Fig. S8(b) (plane 2 nm above rod) and Fig. S8(c) (plane 20 nm above rod) the amplitude modulation in the light scattered near field is almost completely absent whereas it is pronounced in the near fields calculated with the experimental dielectric function (JC).[15]
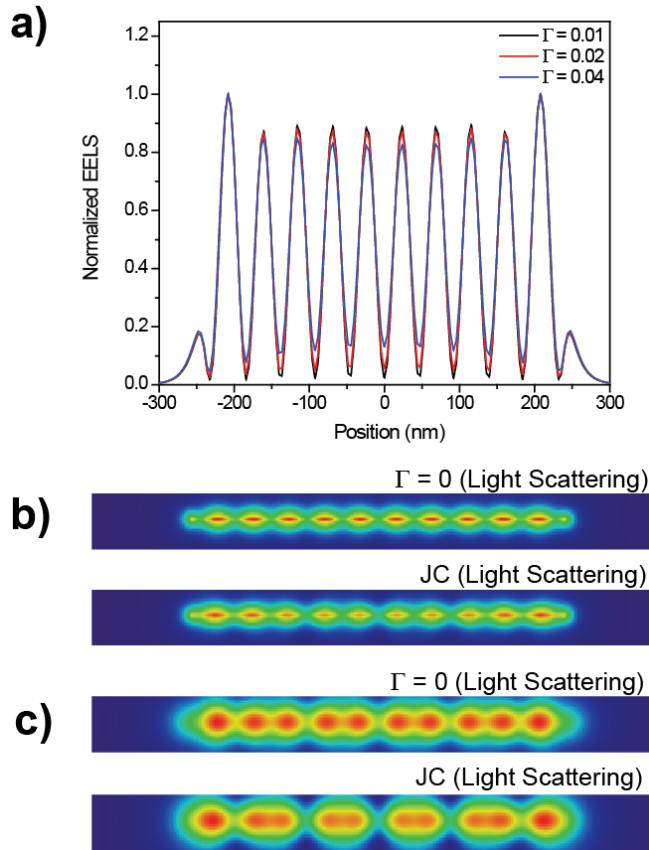
Figure S8. (a) EELS line profiles along a 500 nm long rod (10 nm radius) with varying internal damping parameter calculated with a Drude model dielectric function. (b)-(c) Near fields at planes (b) 2 nm and (c) 20 nm above the rod on resonance with the $m = 11$ mode for this rod. JC refers to the experimental dielectric function from Ref. 15 (SM Sec. 8).

6. Spatial Amplitude Modulation Fitting

As noted in the main text, the spatial amplitude modulation for mode $m = 6$ is not well described

if only $m = 4$ ($n_m - 2$) and $m = 6$ are included in the fit. Figure S9 presents a comparison of fitting

results for $m = 2, 4, 6$ and $m = 4, 6$ only. The intensity at the central peak is under-estimated in

the fit with $m = 4, 6$ whereas if $m = 2$ is also included in the fit, the amplitude modulation is

recovered at all peaks (Fig. 14(c)).
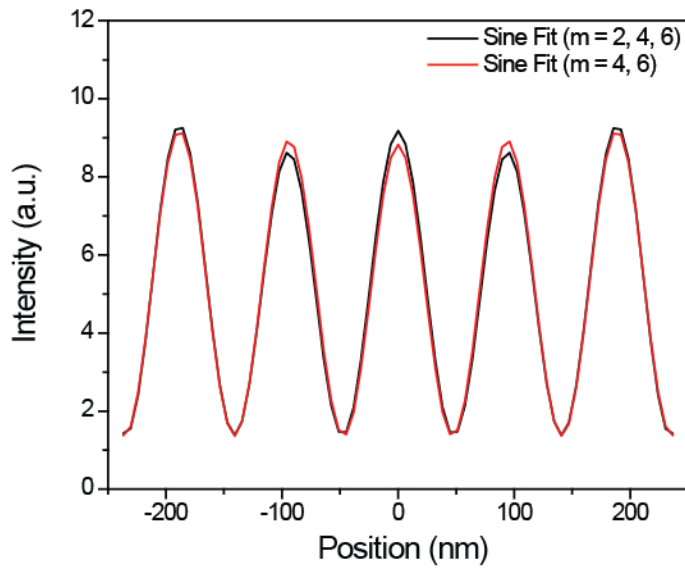
Figure S9. Spatial amplitude modulation fitting of Eq. 4 to simulated $m = 6$ with $m = 2, 4, 6$ and $m = 4, 6$ contributions only.

7. Effect of Rod Length

As noted in Sec. VI of the main text, the length of the nanorod is expected to change the coupling between the longitudinal modes as the modes become increasingly separated in energy as the modes red-shift due to size effects. DDA simulated line profiles for rods 500 nm, 1000 nm, and 1500 in length are presented in Fig. S10. These rods were 10 nm in radius and consisted of 19,955, 40,205, and 60,455 dipoles, respectively. The resonance energies for the $m = 11$ mode were 2.93 eV, 2.11 eV, and 1.62 eV, respectively. Analogously to the effect of internal damping, the 1000 nm and 1500 nm long rods appear to approach a limiting case where mode hybridization is still present but the extent of amplitude modulation changes minimally with increasing separation of the modes in energy.
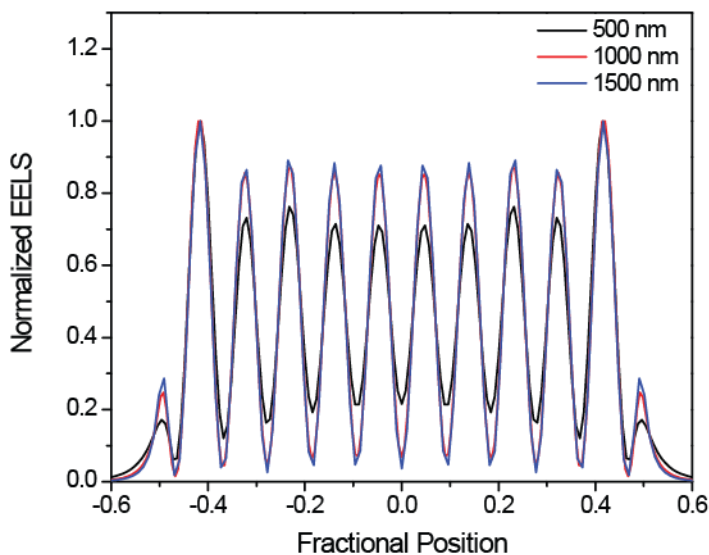
Figure S10. EELS line profiles for mode $m = 11$ for rods 500 nm, 1000 nm, and 1500 nm in length. The incident electron energy is 300 keV.

8. Additional Comments on Related Systems

The computational development of EELS detection of Fano resonances in nanorod dimers,[16] the observation[17] and analysis[18] of hybridization of modes by EELS in silver cubes, and the examination of other Fano-resonant systems with EELS and CL[19,20] establishes EELS as useful tool for probing near field interference effects. In several cases, EELS and CL are directly sensitive to detecting mode hybridization, particularly by examining the spatial modulation of the EELS intensity.[16,17] By energy conservation, the energy loss signal is derived from energy dissipated in the surface plasmon, largely divided into radiative and non-radiative decay pathways.[12] Radiative decay pathways depend on light scattering into the vacuum and will depend on near field interference effects. In the case of interfering modes along a silver nanorod, the induced surface charge will add destructively for some trajectories and constructively for others, giving rise to an observed intensity modulation in a two-dimensional map in addition to effects in the spectral domain. Moreover, the EELS intensity is modulated as a function of probe position by the efficiency of the electron coupling to the particular mode and the field acting back on the electron. While the EELS spectrum includes losses due to plasmon excitations that decay non-radiatively, it is the mode structure and the fields acting back along the electron trajectory that determine the spatial amplitude in EELS maps, resulting in spatially resolved EELS signals that offer insight into the hybridized mode along the rod.

The nanorod case is not dissimilar from the single particle Fano resonant system of a cube on a substrate.[14,17,21] Recent three-dimensional imaging by EELS has demonstrated that EELS records the known corner mode hybridization characteristic of the substrate-induced Fano resonance in plasmonic nanocubes.[17] The peaks in the energy loss spectra are, however, symmetric for the nanocube[17] as they are for the nanorod. Additional analysis of the Fano-resonance or alternately the hybridization of dipolar and quadrupolar modes of the cube by EELS

and EELS simulations by Iberi et al. confirmed the necessary relative phase relationships in electron excitation.[18]

In the case of silver nanorods, the in-phase response recorded in EELS maps of odd modes are qualitatively transferable to analysis of light scattering responses as they correspond to the constructive interference case at the maximum in the far field scattering spectrum. However, the differences identified in near field interactions for even modes, the differences in relative mode excitation, and the resulting differences in spectral line shape and relative contributions of coupled modes introduce new complexity to comparisons of electron microscopy and spectroscopy with light scattering.

9. References

(1)   Egerton, R. F. *Electron Energy-Loss Spectroscopy in the Electron Microscope*; 3rd ed. 2011.; Springer: New York, 2011.

(2)   Aguiar, J. A.; Reed, B. W.; Ramasse, Q. M.; Erni, R.; Browning, N. D. *Ultramicroscopy* **2013**, *124*, 130–138.

(3)   Stöger-Pollach, M. *Micron* **2008**, *39*, 1092–1110.

(4)   Zuloaga, J.; Nordlander, P. *Nano Lett.* **2011**, *11*, 1280–1283.

(5)   Bosman, M.; Ye, E.; Tan, S. F.; Nijhuis, C. A.; Yang, J. K. W.; Marty, R.; Mlayah, A.; Arbouet, A.; Girard, C.; Han, M.-Y. *Sci. Rep.* **2013**, *3*, 1312.

(6)   Vernon, K. C.; Funston, A. M.; Novo, C.; Gómez, D. E.; Mulvaney, P.; Davis, T. J. *Nano Lett.* **2010**, *10*, 2080–2086.

(7)   Zou, C.-L.; Sun, F.-W.; Xiao, Y.-F.; Dong, C.-H.; Chen, X.-D.; Cui, J.-M.; Gong, Q.; Han, Z.-F.; Guo, G.-C. *Appl. Phys. Lett.* **2010**, *97*, 183102.

(8)   Rossouw, D.; Botton, G. A. *Phys. Rev. Lett.* **2013**, *110*, 066801.

(9)   García de Abajo, F. J. *Rev. Mod. Phys.* **2010**, *82*, 209–275.

(10)   López-Tejeira, F.; Paniagua-Domínguez, R.; Rodríguez-Oliveros, R.; Sánchez-Gil, J. A. *New J. Phys.* **2012**, *14*, 023035.

(11)   Liang, H.; Rossouw, D.; Zhao, H.; Cushing, S. K.; Shi, H.; Korinek, A.; Xu, H.; Rosei, F.; Wang, W.; Wu, N.; Botton, G. A.; Ma, D. *J. Am. Chem. Soc.* **2013**, *135*, 9616–9619.

(12)   Sönnichsen, C.; Franzl, T.; Wilk, T.; von Plessen, G.; Feldmann, J.; Wilson, O.; Mulvaney, P. *Phys. Rev. Lett.* **2002**, *88*, 077402.

(13)   Dahmen, C.; Schmidt, B.; von Plessen, G. *Nano Lett.* **2007**, *7*, 318–322.

(14)   Zhang, S.; Bao, K.; Halas, N. J.; Xu, H.; Nordlander, P. *Nano Lett.* **2011**, *11*, 1657–1663.

(15)   Johnson, P. B.; Christy, R. W. *Phys. Rev. B* **1972**, *6*, 4370–4379.

(16)   Bigelow, N. W.; Vaschillo, A.; Camden, J. P.; Masiello, D. J. *ACS Nano* **2013**, *7*, 4511–4519.

(17)   Nicoletti, O.; de la Peña, F.; Leary, R. K.; Holland, D. J.; Ducati, C.; Midgley, P. A. *Nature* **2013**, *502*, 80–84.

(18)   Iberi, V.; Bigelow, N. W.; Mirsaleh-Kohan, N.; Griffin, S.; Simmons, P. D.; Guiton, B. S.; Masiello, D. J.; Camden, J. P. *J. Phys. Chem. C* **2014**, *118*, 10254–10262.

(19)   Lassiter, J. B.; Sobhani, H.; Knight, M. W.; Mielczarek, W. S.; Nordlander, P.; Halas, N. J. *Nano Lett.* **2012**, *12*, 1058–1062.

(20)   Guillaume, S.-O.; Geuquet, N.; Henrard, L. 2011; Vol. 8096, p. 80962E–80962E–7.

(21)   Sherry, L. J.; Chang, S.-H.; Schatz, G. C.; Van Duyne, R. P.; Wiley, B. J.; Xia, Y. *Nano Lett.* **2005**, *5*, 2034–2038.